

Evolution of magnetic phases in SmCrO₃: A neutron diffraction and magnetometric studyMalvika Tripathi, R. J. Choudhary,^{*} and D. M. Phase
*UGC-DAE Consortium for Scientific Research, Indore 452001, India*T. Chatterji and H. E. Fischer
Institut Laue-Langevin, 38042 Grenoble Cedex, France

(Received 23 May 2017; revised manuscript received 16 September 2017; published 17 November 2017)

The classical belief about the mechanism of spin reorientation phase transition (SRPT) and ground-state magnetic structure in SmCrO₃ has become intriguing because of inconsistent bulk magnetization observations. The presence of highly neutron-absorbing Sm atom has so far evaded the determination of microscopic magnetic structure. In the present report, we have utilized very high-energy “hot neutrons” to overcome the Sm absorption and to determine the thermal evolution of magnetic configurations. Unambiguously, three distinct phases are observed: the uncompensated canted antiferromagnetic structure $\Gamma_4(G_x, A_y, F_z; F_z^R)$ occurring below the Néel temperature ($T_N = 191$ K), the collinear antiferromagnetic structure $\Gamma_1(A_x, G_y, C_z; C_z^R)$ occurring below 10 K, and a nonequilibrium configuration with cooccurring Γ_1 and Γ_4 phases in the neighborhood of the SRPT ($10 \text{ K} \leq T \leq 40 \text{ K}$). In differing to the earlier predictions, we divulge the SRPT to be a discontinuous transition where chromium spins switch from the a - b crystallographic plane to the b - c crystallographic plane in a discrete manner with no allowed intermediate configuration. The canting angle of chromium ions in the a - b plane is unusually not a thermal constant, rather it is empirically discerned to follow exponential behavior. The competition between magnetocrystalline anisotropy and free energy derived by isotropic and antisymmetric exchange interactions between different pairs of magnetic ions is observed to govern the mechanism of SRPT.

DOI: [10.1103/PhysRevB.96.174421](https://doi.org/10.1103/PhysRevB.96.174421)**I. INTRODUCTION**

The magnetic properties of rare-earth orthochromites (RCrO₃) have been a customary favorite for researchers to study the variety of complex exchange interactions [1–4]. The interest is rejuvenated because of the recent reports of magnetism-induced ferroelectricity [5,6] and magnetization reversal [7–10]. The prominence of RCrO₃ as a multifunctional material is mainly due to the magnetic ordering temperature, which lies in between the well-studied isostructural families; orthomanganites RMnO₃ ordering at very low temperatures ($T_N < 50$ K) and orthoferrites RFeO₃ ordering at very high temperatures ($T_N > 500$ K) [11–13]. One of the most interesting examples of this family is newly emerging SmCrO₃ where the presence of two magnetic species, Sm and Cr ions, leads to multiple phase transitions, a magnetic glassy phase, and henceforth a very complex magnetic phase diagram [14–16]. SmCrO₃ orders in canted antiferromagnetic structure below the Néel temperature at 191 K (T_N) and the magnetic configuration spontaneously reorients from one easy axis to another, called the spin reorientation phase transition (SRPT) at 34 K (T_{SRPT}). The abrupt SRPT in SmCrO₃ occurring in a very narrow temperature regime ($\Delta T \sim 10$ K) has potential applications in magnetic refrigeration [17,18], thermomagnetic power generation [19], and ultrafast spin switching to modify the speed in recording media [20]. Understanding the mechanism of SRPT plays an important role in the designing of ultrafast switching equipment as well as in learning the fundamental aspects of magnetic interactions. However, there are conflicting reports in the literature regarding the mechanism of spin reorientation and consequent modifications in magnetic structures. Most of the reports [21–25] suggest

the SRPT to be a second-order transition and attribute it to a continuous rotation of Cr³⁺ moments. In bulk magnetization results, a distinct hysteresis during cooling and heating cycles, originating in the vicinity of the SRPT regime, is observed, which broadens up to the Néel temperature, covering a remarkable temperature width of $\Delta T \sim 165$ K in the presence of the applied field $\mu_0 H = 100$ Oe [16,26]. The occurrence of thermal hysteresis and, in addition, the signatures of magnetic glassy phase below T_{SRPT} [16] cannot be explained on the basis of the formerly established second-order nature of the SRPT. On the other hand as a consequence of temperature-dependent isotropic, antisymmetric, and anisotropic exchange interactions among the three pairs Cr³⁺-Cr³⁺, Cr³⁺-Sm³⁺, and Sm³⁺-Sm³⁺ [27], and the anomalous magnetic ground state of the Sm³⁺ ion [28,29], the magnetic phase diagram becomes very complicated. The complexity of the magnetic phase diagram comprising multiple phase transitions is not properly understood so far. One of the key reasons for these discrepancies and the lack of details is the unavailability of experimental insight into the microscopic spin arrangement and magnetic structure.

Neutron diffraction is a useful technique to explore the spin configuration on the microscopic level. Natural Sm contains seven isotopes and the low-energy neutron cross section is dominated by very strong resonance at 0.098 eV of the ¹⁴⁹Sm isotope [30,31]. This strong resonance in ¹⁴⁹Sm occurs because of possible formation of an $S = 3$ bound state in nuclei, resulting in a very high neutron absorption cross section of 42080 b [31,32]. Therefore, compounds containing natural samarium have been mostly disregarded for neutron scattering experiments. To overcome the high absorption, one popular way is to use Sm enriched with an ¹⁵⁴Sm isotope which has a very low-absorption cross section. Unfortunately, the ¹⁵⁴Sm isotope is very costly for synthesizing a sufficient quantity of single-phase polycrystallites. It is observed that the magnitude

^{*}Corresponding author: ram@csr.res.in

of the neutron absorption cross section for the ^{149}Sm isotope reduces significantly if we tune the incident neutron energy to a value much higher than that of the resonance width [30]. Accordingly, using high-energy thermal neutrons or so-called “hot neutrons” provides another good option. Therefore, we recorded diffraction data using the hot source available at the disordered materials diffractometer (D4) [33] at the Institut Laue-Langevin (ILL), Grenoble, France. Although the alternative option of “hot neutrons” has been a remarkable idea for single crystals of Sm containing compounds [34–36], still the literature is entirely lacking in experiments based on polycrystalline or powdered samples because of very high backgrounds and very small moments of Sm atoms. Thanks, however, to the high counting rate and the low background of the D4 instrument, we were able to unambiguously determine the magnetic structures and their evolution with temperature. The observed value of the magnetic moment of Sm ions in SmCrO_3 is anomalously high which has probably helped to improve the data quality.

In this present report we aim to investigate the nature of the SRPT, construct the temperature-driven magnetic phase diagram, and qualitatively understand the mechanism of SRPT in SmCrO_3 .

II. EXPERIMENTAL

The synthesis procedure, phase confirmation by x-ray diffraction (XRD) and valence-state determination of chromium and samarium ions using XPS are reported in Ref. [16,37]. The macroscopic magnetization measurements were carried out using 7T-SQUID-VSM (Quantum Design Inc., USA). Before each measurement, we have reduced the trapped field inside superconducting winding of the electromagnet following the de-Gauss procedure. Temperature-dependent magnetization $M(T)$ measurements were recorded with a 0.5 K/min sweep rate. Neutron diffraction data [38] were collected from the two-axis diffractometer at D4 [33], ILL, Grenoble using a wavelength of 0.4997 Å obtained by reflection of a Cu(220) monochromator. After calibration of the sample, the neutron diffraction intensity was normalized using a standard vanadium sample and corrected for background attenuation, multiple scattering, and inelasticity (Placzek) effects [39]. We measured the spectra at various temperature values ranging from 2 K to 300 K in warming mode without applying the magnetic field. The FULLPROF software package was used for the refinement of the crystal and magnetic structures, wherein we used a value of +5.0 fm for the coherent neutron scattering length of Sm at a wavelength of 0.4997 Å, a value that is consistent with the modeled wavelength dependence as reported by Lynn and Seeger [31]. In particular, BASIRPES [40] was used for generating the irreducible representations and WINPLOTR [41] for simulating the background of the diffraction pattern.

III. RESULTS AND DISCUSSION

Figure 1(a) shows the $M(T)$ curves in zero-field-cooled warming (ZFC), field-cooled cooling (FCC), and field-cooled warming (FCW) cycles with the applied magnetic field $\mu_0 H = 0.05$ T. The first transition at 191 K (T_N) is at-

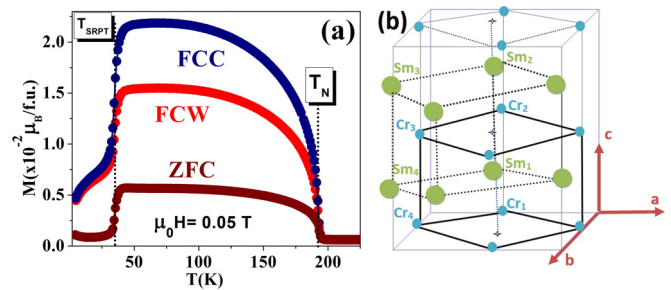


FIG. 1. (a) $M(T)$ curves following ZFC, FCC, and FCW modes in the presence of the applied field $\mu_0 H = 0.05$ T. (b) Crystallographic unit cell of SmCrO_3 .

tributed to the ordering of Cr^{3+} sublattices into the canted antiferromagnetic arrangement due to Dzyaloshinskii-Moriya exchange coupling [42,43]. In rare-earth orthochromites and orthoferrites, commonly the magnetic configuration below T_N is either $\Gamma_2(F_x, C_y, G_z; F_x^R, C_y^R)$ or $\Gamma_4(G_x, A_y, F_z; F_z^R)$ following Bertraut’s notations [44]. If the rare-earth ion is magnetic, then at a particular temperature value ($T < T_N$) the easy axis of magnetization spontaneously changes from one crystallographic direction to another, the phenomenon known as SRPT. In SmCrO_3 the abrupt change in the magnetic moment across 34 K is suggested to be a temperature-driven SRPT [6,21]. SmCrO_3 crystallizes in a distorted orthorhombic perovskite structure with the space group $Pbnm$. One crystallographic unit cell is shown in Fig 1(b), where the nonmagnetic oxygen ions are omitted. Chromium ions occupy the undistorted face centered $4(b)$ Wyckoff positions of the unit cell, whereas the Sm ions are slightly displaced from their $4(c)$ special positions. The distortion is parametrized by $u = 0.00618(19)$ and $v = 0.0616(21)$. The values of u and v were obtained by Rietveld refinement of room-temperature powder XRD data (not shown here) [16].

The thermal evolution of neutron diffraction spectra ranging from 2 K to 300 K is shown in Fig. 2(a). Below T_N , the distinct peak emerges in the regime of $2\theta = 6.44^\circ$. The point-by-point difference spectrum of two patterns, one at room temperature which is above the Néel temperature and another at 2 K, eliminates the effects of external background and multiple scattering caused by the sample holder and the environment [45]. The difference in diffraction patterns, shown in Fig. 2(b), thus represents temperature-dependent phenomena only, caused by magnetic scattering as well as any possible structural modification and the Debye temperature effect at positions of nuclear reflections. As confirmed by powder x-ray diffraction studies [15], there is no structural phase transition at T_N , inferring that the distinct feature at $2\theta = 6.44^\circ$ must be of the magnetic origin. An additional enhancement of intensity is observed at (211) and (113) Bragg’s reflections. The negative contribution in the difference spectrum arises due to the diffuse paramagnetic scattering dominating at room temperature superimposed on the nuclear intensity. A very weak magnetic contribution slightly above the Néel temperature is also observed due to short-range magnetic ordering caused by intrinsic structural distortion in CrO_6 octahedra [46].

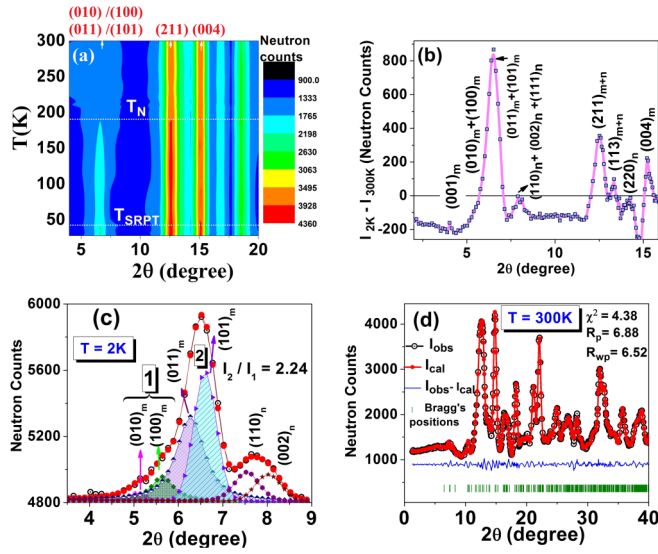


FIG. 2. (a) Thermal evolution of neutron diffraction patterns. (b) The difference in diffraction patterns at 2 K with respect to room temperature. (c) Deconvolution of the magnetic peak at $2\theta = 6.44^\circ$. The subscripts m and n denote magnetic and nuclear planes, respectively. (d) Neutron diffraction pattern at 300 K along with Rietveld-refined pattern of nuclear structure. Hollow circles and solid circles represent the experimentally observed and calculated data points, respectively. The vertical bars denote the Bragg's positions. Solid lines connecting the data points are guides to the eyes.

The asymmetric peak in the regime of $2\theta = 6.44^\circ$ is deconvoluted with four Gaussian peaks and indexed by doublets of closely spaced Bragg's reflections shown as Feature 1: $(100)_m + (010)_m$, and Feature 2: $(101)_m + (011)_m$, in Fig. 2(c).

In the distorted orthorhombic structure $Pbnm$, the a and b axes are slightly unequal and thus the interplaner spacing for the $(011)_m$ and $(101)_m$ planes are slightly different. The very low 2θ difference ($\sim 0.11^\circ$) between the $(011)_m$ and $(101)_m$ planes allows us to safely assume the integrated intensity of Feature 2 as the summation of the individual intensities of two planes. Similarly, the integrated intensity of Feature 1 is denoted as the sum of the individual intensities of the closely spaced planes $(010)_m$ and $(100)_m$ ($\Delta 2\theta \sim 0.09^\circ$).

TABLE I. Structure parameters and reliability indicators obtained from Rietveld refinement of neutron powder diffraction data at 300 K and 2 K. Site occupancy is not considered as a variable during the refinement process.

| | Atoms | Fractional coordinates | | | Thermal parameters | Lattice parameters | Statistical parameters |
|-------|--------|------------------------|------------|------------|--------------------|---|------------------------|
| | | x | y | z | | | |
| 300 K | Sm(4c) | 0.0672(42) | 0.0616(35) | 0.2500 | 0.110(13) | $a = 5.3901(11)$ $b = 5.5424(13)$ $c = 7.6985(15)$ $\chi^2 = 4.25$ | $R_p = 6.35$ |
| | Cr(4b) | 0.500 | 0.0000 | 0.00000 | 0.358(3) | | $R_{wp} = 6.43$ |
| | O1(4c) | 0.0771(85) | 0.4774(87) | 0.2500 | | | $R_{exp} = 3.12$ |
| | O2(8d) | 0.2974(64) | 0.2978(68) | 0.0430(48) | | | |
| 2 K | Sm(4c) | 0.0049(31) | 0.0611(37) | 0.2500 | 0.0785(31) | $a = 5.3836(8)$ $b = 5.5156(14)$ $c = 7.6872(18)$ $\chi^2 = 3.4$ | $R_p = 4.79$ |
| | Cr(4b) | 0.500 | 0.0000 | 0.00000 | 0.125(11) | | $R_{wp} = 4.72$ |
| | O1(4c) | 0.1040(48) | 0.4716(87) | 0.2500 | | | $R_{exp} = 2.56$ |
| | O2(8d) | 0.2928(39) | 0.2864(19) | 0.0484(26) | | | |

The nuclear pattern at 300 K is refined with help of the Rietveld-generated model based on the $Pbnm$ space group as shown in Fig. 2(d), and the obtained structural parameters and reliability indicators are tabulated in Table I. Thermal parameters (or atomic displacement parameters) are related to atomic and electronic vibrations about their mean position, the amount of vibration being quantified by the Debye-Waller parameter. To monitor the procedure of convergence during refinement, the R factors are defined. The first R factor R_{wp} is defined as

$$R_{wp} = \sum_i w_i [y_i(obs) - y_i(cal)]^2 / \sum_i [w_i y_i(obs)]^{1/2} * 100\%.$$

R_{wp} is calculated to provide more weightage to the data points corresponding to Bragg's positions than the background points by including weightage coefficients w_i . The second R factor R_{exp} is defined as

$$R_{exp} = (N - P + C) / \sum_i [w_i y_i(obs)]^{1/2} * 100\%,$$

where N is the total number of observations, P is the number of parameters refined, and C is the number of constraints. The ratio of the square of the above defined R factors gives the χ^2 .

The propagation vector $\mathbf{k} = \mathbf{0}$ has been chosen for generating magnetic structures, which is conventional for RCrO₃ family members [47–49]. The representation theory developed by Bertraut [50,51] reduces the main problem of determining the magnetic structure into identifying irreducible representations (IRs) and the basis functions. In the case of $Pbnm$ (D_{2h}^{16}), there are eight possible one-dimensional (1D) representations, associated with $\mathbf{k} = \mathbf{0}$ wave vector. The general magnetic representation Γ matrix can be written as a linear combination of IRs as

$$\Gamma = 3(\Gamma_1) + 3(\Gamma_3) + 3(\Gamma_5) + 3(\Gamma_7).$$

Only the similar representations can couple if we consider the simultaneous ordering of both Cr³⁺ and Sm³⁺. The symmetry operators, basis functions of IRs, and generated character table corresponding to $Pbnm$ space groups are discussed in the Appendix. The irreducible matrices Γ_i will be denoted as IR(i) in order to avoid confusions arising due to the same conventional notations for IRs and magnetic configurations. Using the simulations for checking the three lowest 2θ

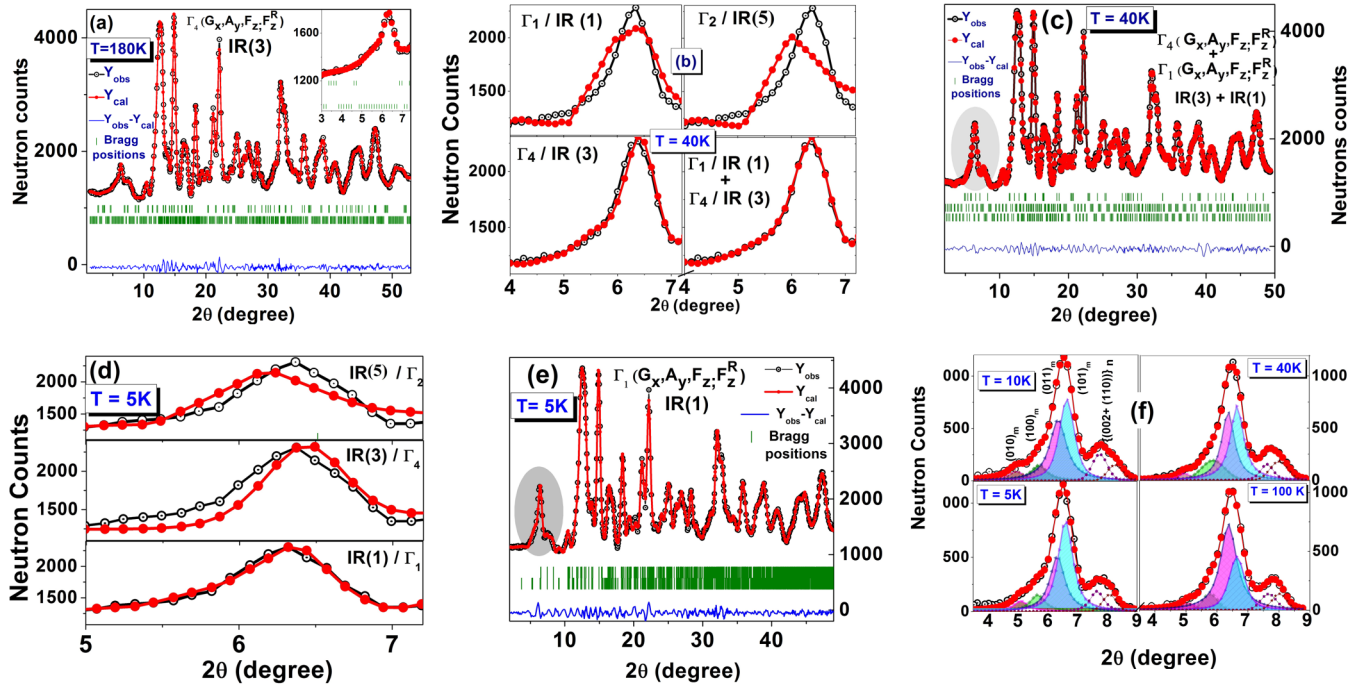


FIG. 3. (a, c, e) Neutron powder diffraction profiles at 180 K, 40 K, and 5 K, respectively, refined with the model pattern generated from Γ_4 , $\Gamma_4 + \Gamma_1$, and Γ_1 magnetic configurations respectively. (b) Comparative view of the magnetic peak fitted with Γ_4 , Γ_2 , Γ_1 , and mixed phases $\Gamma_4 + \Gamma_1$ at 40 K. (d) At $T = 5$ K, the fitted magnetic peak with model Γ_2 , Γ_4 , and Γ_1 configurations. (f) Modification in intensity corresponding to different magnetic Bragg's planes across T_{SRPT} . Hollow circles and solid circles represent the experimentally observed and calculated data points, respectively. The vertical bars denote the Bragg's positions. Solid lines connecting the data points are guides to the eyes.

peaks, (100), (010), and (001), can efficiently reduce the time and effort in the assignment of unambiguous IRs [52]. The simulation results corresponding to all possible IRs are described in the Appendix.

The neutron powder diffraction pattern is Rietveld refined with model crystal and magnetic structure to further resolve the magnetic structure and to estimate structure parameters and magnetic moments of ordered Cr and Sm atoms. It is observed from the refinement at 180 K (below T_N) that the magnetic structure can be uniquely determined with IR(3) and $\mathbf{k} = (0,0,0)$ propagation vector, the spin mode belonging to the $\Gamma_4(G_x, A_y, F_z; F_z^R)$ magnetic configuration [Fig. 3(a)]. The Γ_4 magnetic configuration is observed to be the suitable magnetic structure for all temperature values lying in between $40 \text{ K} < T < T_N$. As we lower the temperature approaching the SRPT regime, IR(3) no longer provides a reliable match in between experimental and Rietveld-generated model patterns. As shown in Figs. 3(b) and 3(c), for an agreeable match with experimental data recorded at 40 K, we have to add an additional magnetic phase defined by IR(1) or the $\Gamma_1(A_x, G_y, C_z; C_z^R)$ magnetic configuration in the calculated pattern. The two phases are observed to coexist for all temperature values ranging from 10 K to 40 K and the magnetic structure completely transforms into the $\Gamma_1(A_x, G_y, C_z; C_z^R)$ configuration below 10 K, which is a collinear antiferromagnetic structure [Figs. 3(d) and 3(e)]. To visualize a clear picture of the asymmetry variation in the magnetic peak at $2\theta = 6.44^\circ$ in the SRPT regime, we fitted the diffraction patterns ranging from 3.5° to 9.0° with six peaks as shown in Fig. 3(f). The full widths at half maximum of all

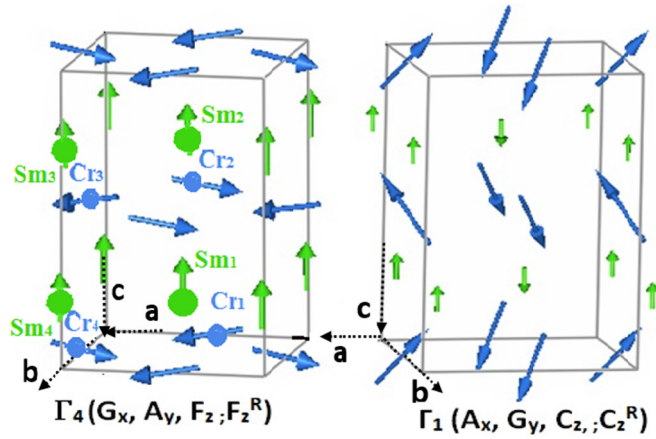
the peaks are maintained to a constant value which is close to instrumental resolution. The variation in intensity therefore clearly demonstrates the ordering process across the SRPT. The following modifications in the diffraction pattern below T_{SRPT} can be observed:

(i) The ratio of $(011)_m$ and $(101)_m$ is changed: It is evident that the magnetic intensity corresponding to the $(011)_m$ plane is more intense than that of the $(101)_m$ plane for temperatures above T_{SRPT} . However, this arrangement is reversed below T_{SRPT} , where the $(101)_m$ plane becomes more intense. The transfer of intensity from the $(011)_m$ plane to the $(101)_m$ plane is a clear indication of the spin reorientation phase transition [53].

(ii) The intensities related to the $(010)_m$ and $(100)_m$ planes significantly increase below 40 K. The emergence of the $(010)_m$ and $(100)_m$ planes correspond to the ordering of the Sm moments [47].

The spin configurations corresponding to the Γ_4 and Γ_1 structures are illustrated in Fig. 4. In the $\Gamma_4(G_x, A_y, F_z; F_z^R)$ antiferromagnetic structure, the magnetic moments on neighboring atomic sites point exactly opposite to each other along the $x \parallel a$ and $y \parallel b$ directions, whereas the $z \parallel c$ components are parallel, giving rise to a weak ferromagnetism along the c axis. Very small canting with respect to the $z \parallel c$ axis results in a small $(0.18\text{--}0.39 \mu_B)$ uncompensated moment along the c axis. Γ_1 is a collinear antiferromagnetic structure not allowing any uncompensated moments.

Most of the earlier reports [21,23,24] have predicted that the SRPT in SmCrO_3 is characterized by the continuous rotation of Cr^{3+} and Sm^{3+} magnetic moments from high-temperature


 FIG. 4. Schematic of the Γ_4 and Γ_1 spin configurations.

$\Gamma_4(G_x, A_y, F_z; F_z^R)$ to low-temperature $\Gamma_2(F_x, C_y, G_z; F_x^R, C_y^R)$ ground states. The basis of this belief was based on acoustic velocity measurements [21] and theoretical DFT calculations [23]. In contrast to the earlier predictions our observation suggests the coexistence of Γ_4 and Γ_1 phases in the vicinity of the SRPT. When the latent heat is involved in a phase transition process, say in crystallization of a high-temperature phase into a low-temperature phase, the system has to exchange the energy from its surroundings to complete the transformation. During the process, some of the high-temperature supercooled clusters in the metastable state can survive in the background of the transformed low-temperature phase even below the transition temperature. The transformation is fully completed when the temperature becomes less than the supercooling temperature, below which the metastable state is no more a local minima of energy. Thus the phase coexistence is an intrinsically associated phenomenon with the occurrence of a first-order phase transition. The phase coexistence in the vicinity of the SRPT reveals the discontinuous nature of the transition. The coexisting phases and the collinear antiferromagnetic ground state $\Gamma_1(A_x, G_y, C_z; C_z^R)$ at 5 K are also in accordance with the behavior of magnetic isotherms at 25 K and 5 K as shown in Fig. 5(a). The presence of weak ferromagnetic Γ_4 clusters below T_{SRPT} originates the hysteresis curves with significant coercivity at 25 K, whereas magnetic isotherms transform into straight lines at 5 K akin to the collinear antiferromagnetic ground state.

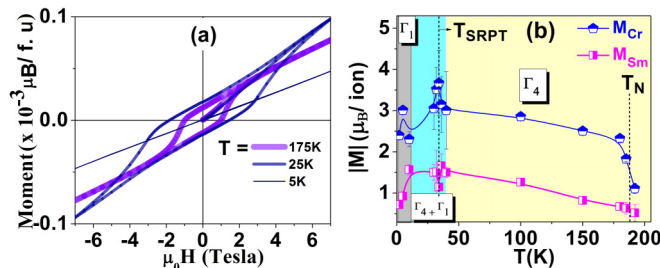


FIG. 5. (a) Magnetic isotherms measured at various temperatures. (b) Variation of magnetic moments with temperature and phase diagram in temperature space.

The total magnitude of chromium and samarium ionic moments obtained from the refinement of the neutron powder diffraction at different temperatures are shown in Fig. 5(b). The observed value of the moment of samarium ions is exceptionally larger than expected, $gJ\mu_B = 0.86$ for Sm^{3+} ions. In the case of Sm^{3+} , spin and orbital angular moments are coupled in an antiparallel fashion because of the spin-orbit interaction. The presence of closely spaced excited multiplet levels with angular moments $J = 7/2$ and $J = 9/2$ also influences the population in the ground state with the angular momentum $J = 5/2$ [54,55] and henceforth the magnetic moment is expected to be enhanced [56]. In some intermetallic compounds, a significant reduction in the Sm moment is also observed due to conduction electron polarization introduced by lattice distortion or geometrical frustration [28,34]. SmCrO_3 is a Mott-type insulator [15] in which the magnetic moment is governed only by the J -level mixing and the Sm-Cr exchange interaction. The noticeable drop in Sm^{3+} moments in the Γ_1 phase suggests the nonuniform modifications in spin and orbital angular moments in such a way to reduce the total angular momentum. The possible origins of the observed decrement in moments are the following: (i) the distortion in CrO_6 octahedra below T_{SRPT} [15] and henceforth the change in crystal field splitting and spin-orbit interaction, and (ii) moderate modifications in the exchange field at Sm^{3+} cite due to changes in chromium magnetic configurations.

IV. ANALYSIS

The integrated intensity variation of Feature 2 is shown in Fig. 6(a). The Feature 2 intensity profile is fitted with the power law $I = I_0(1 - T/T_C)^{2\beta}$ in the Γ_4 phase, where I is the integrated intensity of the magnetic peak, I_0 is the proportionality constant, T_C is the critical temperature, and β is the power exponent [57,58]. The value of the power exponent β is found to be 0.48(9) which suggests that the mean-field theory is valid in the vicinity of T_N . The variation of canting angles ϕ , ψ , and χ projected over the crystallographic a , b , and c axes, respectively, with respect to temperature is shown in Fig. 6(b). The canting angle χ over the $z \parallel c$ axis is a characteristic of a particular magnetic phase as it remains approximately constant with temperature. However, the moment is systematically rotating in the a - b plane with thermal variations in both the Γ_4 and Γ_1 phases. The direction of the moment tends to move towards the a axis while lowering the temperature in the Γ_4 phase, whereas the tendency to align along the b axis is observed in the Γ_1 axis. The canting angle ϕ in Γ_4 is empirically found to vary in an exponential manner, $\phi = \phi_0 + A\exp(\alpha T)$.

Various phenomenological and microscopic approaches are designed to analyze the SRPT observed in orthochromites and orthoferrites employing the free energy of the system to control the easy axis rotation. Horner and Verma [59] have utilized Landau's theory of second-order phase transition to describe the free energy with the direction of easy axis with respect to the z axis (θ) as an order parameter and anisotropy constants as temperature-dependent linear coefficients (η_2 and η_4):

$$f(\theta) = \eta_0 + \eta_2 \cos \theta + \eta_4 \cos^2 \theta. \quad (1)$$

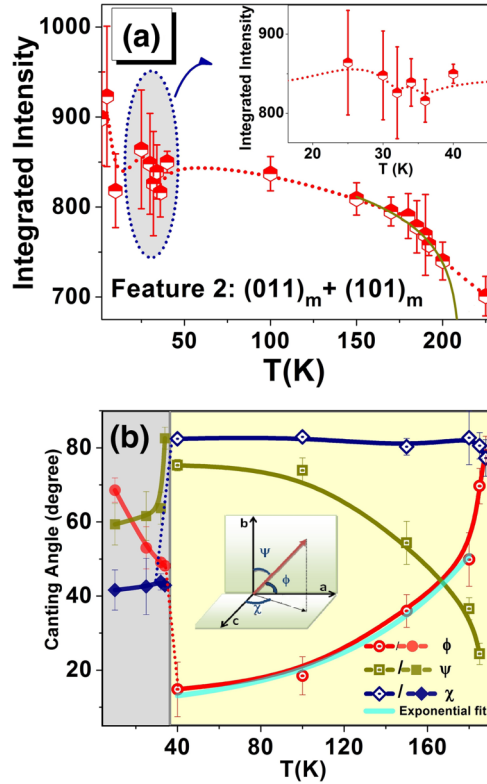


FIG. 6. (a) Variation of integrated intensities corresponding to Feature 2: $(011)_m + (101)_m$. The integrated intensity profile is fitted with the power law behavior $I = I_0(1 - T/T_C)^{2\beta}$ in the vicinity of T_N . The inset shows the integrated intensity variation in the neighborhood of the SRPT. (b) Evolution of canting angles with respect to temperature in the Γ_4 and Γ_1 phases. The inset illustrates the nomenclature of angles with respect to the crystallographic axes.

The minimization of the free energy gives three possible orientations for the easy axis: $\theta = 0$, $\theta = \pi/2$, and $\sin^2\theta = -\eta_2/2\eta_4$. If η_2 is positive, the third solution is real, thus describing a case of continuous rotation of the easy axis from 0 to $\pi/2$. On the other hand, if η_2 is negative, all the intermediate values between 0 and $\pi/2$ are imaginary, suggesting that θ should abruptly jump from 0 to $\pi/2$, which is the case of first-order spin-flop transition. In this present report we follow the approach of Yamaguchi [27], considering the antisymmetric and anisotropic exchange interactions between Sm^{3+} and Cr^{3+} as the key ingredient for the SRPT. As shown in Fig. 7, ϕ is the representative canting angle of Cr moments in Γ_4 configurations, respectively, with respect to the $a \parallel x$ crystallographic axis. The effective field due to isotropic exchange interaction between Cr_1 and Cr_2 ions per unit $g\mu_B$ is

$$F_{\text{Cr}_1, \text{Cr}_2} = J_1 |M_{\text{Cr}_1}| |M_{\text{Cr}_2}| \cos \beta, \quad (2)$$

which is acting along the c axis. Similarly, the total effective field due to isotropic exchange interactions between all Cr-Cr pairs can be written as

$$F_{\text{Cr}_1 - \text{Cr}_4, z} = 2(J_1 + J_2) |M_{\text{Cr}_1}| |M_{\text{Cr}_2}| \cos \beta, \quad (3)$$

where J_1 and J_2 are the isotropic exchange constants for Cr^{3+} - Cr^{3+} exchange interactions and β is the angle between

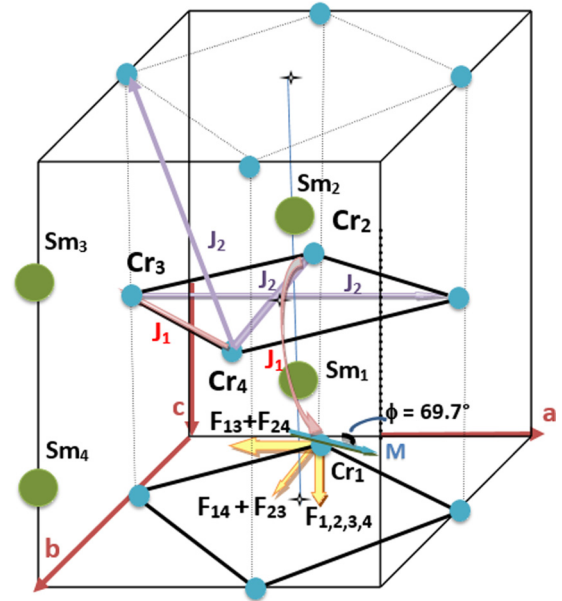


FIG. 7. Schematic illustration of isotropic exchange interactions between chromium ions and effective fields corresponding to antisymmetric exchange interactions caused by Sm^{3+} ions acting on chromium moments.

the magnetic moments of two chromium ions. J_1 is the mean value of the two exchange constants for six neighboring Cr^{3+} ions along the $a \pm b$ and c directions and J_2 is the mean value of three exchange constants for the 12 Cr^{3+} ions, as illustrated in Fig. 7. In the approximation of molecular field theory, J_1 and J_2 are related to the Néel temperature and the Curie-Weiss temperature as [60]

$$\begin{aligned} T_C &= 2S(S+1)(6J_1 + 12J_2)/3k, \\ T_N &= 2S(S+1)(-6J_1 + 12J_2)/3k. \end{aligned}$$

The estimated value of the exchange constants are $J_1/k = -19.48 \text{ cm}^{-1}$ and $J_2/k = -6.68 \text{ cm}^{-1}$. The isotropic interaction fields at chromium sites due to Sm^{3+} moments can be written in a very similar way, replacing J_1 and J_2 with the exchange coefficient \bar{J} corresponding to the Sm-Cr interaction. According to Yamaguchi's model, the magnetic interaction with Sm^{3+} spins produces two sets of antisymmetric effective fields on the Cr^{3+} spins along the crystallographic axis. The effective field arising due to antisymmetric exchange interaction has components along the a and b axes. As the magnetic configuration along the $a \parallel x$ crystallographic direction follows G -type ordering, the contributions from only nonconsecutive pairs of chromium (1,3) and (2,4) are added up. Similarly only alternate pairs of chromium ions (1,4) and (2,3) will contribute to the total effective field along the $b \parallel y$ axis where the C -type magnetic ordering is followed. The total effective field because of the antisymmetric exchange interaction along the $a \parallel x$ axis is given as

$$F_{\text{Cr}_1 \text{Sm}_3} + F_{\text{Cr}_2 \text{Sm}_4} = -2(\kappa_x + \kappa'_x) |M_{\text{Cr}}| |M_{\text{Sm}}| \sin \phi, \quad (4)$$

and along the $b \parallel y$ axis it is given as

$$F_{\text{Cr}_1 \text{Sm}_4} + F_{\text{Cr}_2 \text{Sm}_3} = 2(\kappa_y + \kappa'_y) |M_{\text{Cr}}| |M_{\text{Sm}}| \sin \chi, \quad (5)$$

where κ_i and κ'_i denote the i th components of the antisymmetric exchange interaction coefficients between first and second nearest Sm³⁺ neighbors for Cr³⁺ ions, respectively. The total energy corresponding to these effective fields is

$$E_{\Gamma_4} = 2|M_S m|[-(\kappa_x + \kappa'_x)M_{Cr_x} \sin \phi + (\kappa_y + \kappa'_y)M_{Cr_y} \sin \chi + 2\bar{J}M_{Cr_z} \cos \psi]g\mu_B. \quad (6)$$

From the literature, the average value of κ_i in the Γ_4 spin configuration is 0.1646 erg/mol and \bar{J} is 0.132 K [21,61]. Since we have assumed that the polarized Sm³⁺ spin points exactly towards the effective field direction and has no component along the x axis or the y axis, the antisymmetric exchange interaction Sm³⁺-Cr³⁺ lies in the a - b plane, thus $\kappa_z = 0$. For the sake of simplicity we replace the value of κ_y and κ'_y by $\langle \kappa_i \rangle / 2$. This assumption is valid in the present case since the distortion of Sm atoms from ideal positions is very small. The estimated total free energy just below the Néel temperature, parametrized with $T = 185$ K, $\phi = 69.7^\circ$, $\psi = 25.54^\circ$, and $\chi = 79.85^\circ$, is $= 0.1355 \times 10^6$ erg/mol, and just before T_{SRPT} at $T = 40$ K, $\phi = 14.72^\circ$, $\psi = 75.23^\circ$, and $\chi = 82.63^\circ$, it is equal to 0.976×10^6 erg/mol. Typically the magnetocrystalline energy associated with the Cr³⁺-Cr³⁺ system is 10^6 erg/mol [1]. In the temperature regime close to the SRPT, the total free energy due to exchange interactions between Sm³⁺ and Cr³⁺ and the anisotropy energy are almost equivalent and thus any further decrement in temperature can reorient the system in another possible configuration. Therefore, we consider the SRPT in SmCrO₃ as an effect of the competing structural anisotropy energy and the exchange interactions between chromium and samarium ions.

V. CONCLUSION

We have performed powder neutron diffraction measurements to determine the controversial magnetic structure, exploiting the $\lambda = 0.4997$ Å hot neutrons. Direct evidence of the discontinuous-type spin reorientation phase transition is presented, the chromium moments turning over from the c -axis uncompensated antiferromagnetic structure Γ_4 to the compensated collinear antiferromagnetic ground state Γ_1 . The anomalously high Sm moment and the exponential variation of the canting angles with temperature are unique observations. The functional behavior of the isotropic and antisymmetric exchange energy with the temperature and

the canting angle is elaborated to play a major role in the mechanism of SRPT.

ACKNOWLEDGMENT

M.T. thanks Dr. C. M. N. Kumar for help in understanding the refinement process.

APPENDIX

In the representation theory developed by Bertraut [50,51,62], the transformation properties of a magnetic structure under the classical symmetry operations of the space groups are considered. We first generate a reducible representation matrix of the space group from the transformation matrices and basis vectors which are able to describe the magnetic structure.

For the $Pbnm$ space group (D_{2h}^{16}) the generators are two screw axes, $2_{1,x}$ at $(x, 0.25, 0)$ and $2_{1,y}$ at $(0.25, y, 0.25)$, and the symmetry center $\bar{1}$ at $(0,0,0)$. The point group related to the crystal structure has four symmetry elements: e , 2_x , 2_y , and $2_z = 2_x 2_y$.

For D_{2h}^{16} , the magnetic and chemical unit cells are identical; i.e., the wave vector associated with the magnetic structure is $\mathbf{k} = (0,0,0)$. The full point group symmetry of the magnetic space group consists of eight symmetry elements, four unprimed and four primed operators:

$$e, 2_x, 2_y, 2_z, e.1' = 1', 1'.2_x = 2'_x, 1'.2_y = 2'_y, 1'.2_z = 2'_z.$$

There is one 1D irreducible representation associated with each of the symmetry operators and henceforth there are eight irreducible 1D representations associated with $\mathbf{k} = 0$ and the $Pbnm$ space group. The generated character table for each irreducible representation along with the corresponding spin modes for chromium and samarium are tabulated in Table II. F_i , A_i , C_i , and G_i ($i = x, y, z$) are the components of the base vectors characterizing the spin modes: ferromagnetic arrangement ($+++$) and antiferromagnetic arrangements ($+ - - +$), ($+ + - -$), and ($+ - + -$), respectively. The atomic positions of the Cr₁₋₄ and Sm₁₋₄ atoms are defined as Cr₁ = $(0.5, 0, 0)$, Cr₂ = $(-0.5, 0, 0.5)$, Cr₃ = $(1.0, 0.5, 0)$, Cr₄ = $(0, 0.5, 0)$, Sm₁ = $(0.05, 0.06, 0.25)$, Sm₂ = $(0.99, 0.94, 0.75)$, Sm₃ = $(0.51, 0.44, 0.75)$, Sm₄ = $(0.51, 0.44, 0.75)$ at 2 K, as illustrated in Fig. 1(b). The eight magnetic groups listed in Table II are not all distinct. We can consider only four of

TABLE II. Character table generated for the $Pbnm$ space group with $\mathbf{k} = 0$.

| IR | Generators | | | Spin modes | | Magnetic moments at atomic positions | | | | | | | Space group | |
|-------------------|------------|-----------|-----------|-----------------|------------|--------------------------------------|-----------------|-----------------|-----------------|-----------------|-----------------|-----------------|--------------|-----------------|
| | $2_{1,x}$ | $2_{1,y}$ | $\bar{1}$ | Cr(4b) | Sm(4c) | Cr ₁ | Cr ₂ | Cr ₃ | Cr ₄ | Sm ₁ | Sm ₂ | Sm ₃ | | Sm ₄ |
| IR(1)/ Γ_1 | + | + | + | A_x, G_y, C_z | C_z | (u, v, w) | $(-u, -v, w)$ | $(u, -v, -w)$ | $(-u, v, -w)$ | $(0, 0, n)$ | $(0, 0, n)$ | $(0, 0, -n)$ | $(0, 0, -n)$ | $Pbnm$ |
| IR(2) | + | - | + | A_x, G_y | A_x, G_y | | | | | $(l, m, 0)$ | $(-l, -m, 0)$ | $(l, -m, 0)$ | $(-l, m, 0)$ | $Pbn'm'$ |
| IR(3)/ Γ_4 | - | + | + | G_x, A_y, F_z | F_z | (u, v, w) | $(-u, -v, w)$ | $(-u, v, w)$ | $(u, -v, w)$ | $(0, 0, n)$ | $(0, 0, n)$ | $(0, 0, n)$ | $(0, 0, n)$ | $Pb'nm'$ |
| IR(4) | - | - | + | G_x, A_y | G_x, A_y | | | | | $(l, m, 0)$ | $(-l, -m, 0)$ | $(-l, m, 0)$ | $(l, -m, 0)$ | $Pb'n'm'$ |
| IR(5)/ Γ_2 | + | + | - | F_x, C_y, G_z | F_x, C_y | (u, v, w) | $(u, v, -w)$ | $(u, -v, -w)$ | $(u, -v, w)$ | $(l, m, 0)$ | $(l, m, 0)$ | $(l, -m, 0)$ | $(l, -m, 0)$ | $Pb'n'm'$ |
| IR(6) | + | - | - | G_z | G_z | | | | | $(0, 0, -n)$ | $(0, 0, n)$ | $(0, 0, n)$ | $(0, 0, n)$ | $Pb'nm$ |
| IR(7)/ Γ_3 | - | + | - | C_x, F_y, A_z | C_x, F_y | (u, v, w) | $(u, v, -w)$ | $(-u, v, w)$ | $(u, v, -w)$ | $(l, m, 0)$ | $(l, m, 0)$ | $(-l, m, 0)$ | $(-l, m, 0)$ | $Pbn'm$ |
| IR(8) | - | - | - | A_z | A_z | | | | | $(0, 0, n)$ | $(0, 0, -n)$ | $(0, 0, n)$ | $(0, 0, -n)$ | $Pbnm'$ |

TABLE III. Simulation results showing the possible magnetic reflections for different IRs allowed by symmetry.

| $(001)_m$ | $(010)_m$ and $(100)_m$ | $(011)_m$ and $(101)_m$ |
|-----------|-------------------------|----------------------------|
| IR(1) | IR(5), IR(7), IR(1) | IR(3), IR(5), IR(7), IR(1) |

them as unique representations. The corresponding magnetic structure is also listed along with the representation matrices.

In general the magnetic moment of an atom indexed as j in the l th unit cell, in any magnetic structure, can be written in the form of a Fourier series as

$$m_{lj} = \sum_k S_{kj} \exp(-2\pi i \mathbf{k} \cdot \mathbf{R}_l),$$

where \mathbf{k} and \mathbf{R}_l are the vectors referred to the reciprocal space and the direct crystallographic basis, respectively. S_{kj} are the Fourier components of the magnetic moments. Considering the symmetry of the crystal structure, the Fourier coefficients S_{kj} can be written as

$$S_{kj} = \sum_n C_n^{\mathbf{k}v} \psi_n^{\mathbf{k}v},$$

where $C_n^{\mathbf{k}v}$ are the coefficients of the linear combination and $\psi_n^{\mathbf{k}v}$ are the basis vectors corresponding to the irreducible representation. The index n varies from 1 to the dimension of the irreducible representations [63,64].

For structures with $k = (0,0,0)$, the magnetic moments of the Cr ions in a unit cell are described by the Fourier coefficients as $M_{0j} = S_{0j}$. For $\mathbf{k} = 0$, the magnetic structure can be globally described by Fourier coefficients which

coincide with the whole set of magnetic moments:

$$m_{[1,2,3,4]} = S_{[k]} = u\psi_1^{\mathbf{k}v} + v\psi_2^{\mathbf{k}v} + w\psi_3^{\mathbf{k}v},$$

where $C_n^{\mathbf{k}v} = (u, v, w)$ are the mixing coefficients. These coefficients can be interpreted as matrices corresponding to the transformation of the magnetic moment of the atom. Similarly, the mixing coefficients for the Sm ions are denoted as (l, m, n) .

To generate the representation matrix, we have used the BASIRPES program [40], which leads to four allowed spin configurations for Cr atoms at $4b$ Wyckoff positions and eight possible spin configurations for Sm at $4c$ Wyckoff positions. The possible magnetic structures along with the components of magnetic moments for Cr and Sm atomic sites are listed in Table II. We have used FULLPROF to generate simulated intensity patterns corresponding to all four IRs at $T = 100$ K. Different IRs contribute to different combinations of allowed planes and corresponding intensities of the $(001)_m$, $(010)_m/(100)_m$, and $(011)_m/(101)_m$ planes. The allowed planes corresponding to the IRs are listed in Table III. The following points can be noted on the comparison of the observed diffraction patterns and the simulation results: (i) There is negligible intensity corresponding to $(010)_m/(100)_m$ in the observed diffraction pattern at 100 K which excludes the possibility of all the other IRs except IR(3) or the Γ_4 configuration. (ii) Below T_{SRPT} , a significant increment in intensity corresponding to the $(010)_m$ and $(100)_m$ peaks is observed. In addition, we also observe the presence of $(001)_m$ below T_{SRPT} , although the peak intensity is very weak but higher-angle parallel planes with comparatively higher intensities are clearly visible. As a further confirmation, it is observed that the neutron diffraction pattern for all T ranging from 40 K to T_N provides the most reliable match with the Rietveld-refined pattern generated with model IR(3) or the Γ_4 magnetic configuration.

-
- [1] A. H. Cooke, D. M. Martin and M. R. Wells, *J. Phys. C : Solid state Phys.* **7**, 3133 (1974).
- [2] A. Hasson, R. Hornreich, Y. Komet, B. Wanklyn, and I. Yaeger, *Phys. Rev. B* **12**, 5051 (1975).
- [3] R. Hornreich, Y. Komet, R. Nolan, B. Wanklyn, and I. Yaeger, *Phys. Rev. B* **12**, 5094 (1975).
- [4] J. Gordon, R. Hornreich, S. Shtrikman, and B. Wanklyn, *Phys. Rev. B* **13**, 3012 (1976).
- [5] D. Khomskii, *J. Magn. Magn. Mater.* **306**, 1 (2006).
- [6] B. Rajeswaran, D. I. Khomskii, A. K. Zvezdin, C. N. R. Rao, and A. Sundaresan, *Phys. Rev. B* **86**, 214409 (2012).
- [7] K. Yoshii, *J. Solid State Chem.* **159**, 204 (2001).
- [8] K. Yoshii, *Mater. Res. Bull.* **47**, 3243 (2012).
- [9] K. Yoshii, *Appl. Phys. Lett.* **99**, 142501 (2011).
- [10] Y. Cao, S. Cao, W. Ren, Z. Feng, S. Yuan, B. Kang, B. Lu, and J. Zhang, *Appl. Phys. Lett.* **104**, 232405 (2014).
- [11] H. Sugie, N. Iwata, and K. Kohn, *J. Phys. Soc. Jpn.* **71**, 1558 (2002).
- [12] T. Kimura, G. Lawes, T. Goto, Y. Tokura, and A. P. Ramirez, *Phys. Rev. B* **71**, 224425 (2005).
- [13] J.-S. Zhou and J. B. Goodenough, *Phys. Rev. B* **77**, 132104 (2008).
- [14] M. El Amrani, M. Zaghrioui, V. T. Phuoc, F. Gervais, and N. E. Massa, *J. Magn. Magn. Mater.* **361**, 1 (2014).
- [15] A. Ghosh, K. Dey, M. Chakraborty, S. Majumdar, and S. Giri, *Europhys. Lett.* **107**, 47012 (2014).
- [16] M. Tripathi, R. Choudhary, and D. Phase, *RSC Adv.* **6**, 90255 (2016).
- [17] M. Ohkoshi, H. Kobayashi, T. Katayama, M. Hirano, and T. Tsushima, *Jpn. J. Appl. Phys.* **15**, 2019 (1976).
- [18] M. Ohkoshi, H. Kobayashi, T. Katayama, M. Hirano, and T. Tsushima, *IEEE Trans. Magn.* **13**, 1158 (1977).
- [19] D. Rocco, J. Amaral, J. Leitão, V. Amaral, M. Reis, S. Das, R. Fernandes, J. Araújo, A. Pereira, P. Tavares *et al.*, *J. Phys. D: Appl. Phys.* **42**, 055002 (2009).
- [20] A. Kimel, B. Ivanov, R. Pisarev, P. Usachev, A. Kirilyuk, and T. Rasing, *Nat. Phys.* **5**, 727 (2009).
- [21] G. Gorodetsky, R. Hornreich, S. Shaft, B. Sharon, A. Shaulov, and B. Wanklyn, *Phys. Rev. B* **16**, 515 (1977).
- [22] G. Gorodetsky, S. Shaft, A. Shaulof, B. Wanklyn, B. Sharon, I. Yaeger, J. Becker, G. Lander, and J. Rhyne, *AIP Conf. Proc.* **29**, 449 (1976).
- [23] X. Qian, L. Chen, S. Cao, and J. Zhang, *Solid State Commun.* **195**, 21 (2014).
- [24] S. Huang, L. Shi, Z. Tian, H. Sun, and S. Yuan, *J. Magn. Magn. Mater.* **394**, 77 (2015).
- [25] X.-L. Qian, J. Kang, B. Lu, S.-X. Cao, and J.-C. Zhang, *RSC Adv.* **6**, 10677 (2016).

- [26] S. Lei, L. Liu, C. Wang, C. Wang, D. Guo, S. Zeng, B. Cheng, Y. Xiao, and L. Zhou, *J. Mater. Chem. A* **1**, 11982 (2013).
- [27] T. Yamaguchi, *J. Phys. Chem. Solids* **35**, 479 (1974).
- [28] H. Adachi and H. Ino, *Nature (London)* **401**, 148 (1999).
- [29] J. Schweitzer, *Phys. Rev. B* **13**, 3506 (1976).
- [30] P. De Bievre and P. Taylor, *Int. J. Mass Spectrom. Ion Processes* **123**, 149 (1993).
- [31] J. Lynn and P. Seeger, *At. Data. Nucl. Data Tables* **44**, 191 (1990).
- [32] V. F. Sears, *Neutron News* **3**, 26 (1992).
- [33] H. Fischer, G. Cuello, P. Palleau, D. Feltn, A. Barnes, Y. Badyal, and J. Simonson, *Appl. Phys. A: Mater. Sci. Process.* **74**, s160 (2002).
- [34] J. Pospíšil, G. Nénert, S. Miyashita, H. Kitazawa, Y. Skourski, M. Diviš, J. Prokleška, and V. Sechovský, *Phys. Rev. B* **87**, 214405 (2013).
- [35] C.-Y. Kuo, Y. Drees, M. Fernández-Díaz, L. Zhao, L. Vasylychko, D. Sheptyakov, A. Bell, T. Pi, H.-J. Lin, M.-K. Wu *et al.*, *Phys. Rev. Lett.* **113**, 217203 (2014).
- [36] D. Givord, J. Laforest, J. Schweizer, and F. Tasset, *J. App. Phys.* **50**, 2008 (1979).
- [37] M. Tripathi, R. J. Choudhay, A. Wadikar, and D. M. Phase, *AIP Conf. Proc.* **1832**, 090027 (2017).
- [38] T. Chatterji and H. E. Fischer, Tests of d4's new cryofurnace on a weakly-scattering and highly absorbing magnetic sample (sm-containing), Report, Institut Laue-Langevin (ILL), 2016 .
- [39] H. E. Fischer, A. C. Barnes, and P. S. Salmon, *Rep. Prog. Phys.* **69**, 233 (2006).
- [40] J. Rodriguez-Carvajal, *Solid State Phenom.* **170**, 263 (2011).
- [41] T. Roisnel and J. Rodríguez-Carvajal, in *Materials Science Forum* (Transtech, Switzerland, 1999), Vol. 378, pp. 118–123.
- [42] I. Dzyaloshinsky, *J. Phys. Chem. Solids* **4**, 241 (1958).
- [43] T. Moriya, *Phys. Rev.* **120**, 91 (1960).
- [44] E. Bertaut, G. Bassi, G. Buisson, P. Burlet, J. Chappert, A. Delapalme, J. Mareschal, G. Rault, R. Aleonard, R. Pauthenet *et al.*, *J. Appl. Phys.* **37**, 1038 (1966).
- [45] E. Wollan and W. Koehler, *Phys. Rev.* **100**, 545 (1955).
- [46] J.-S. Zhou, J. A. Alonso, V. Pomjakushin, J. B. Goodenough, Y. Ren, J.-Q. Yan, and J.-G. Cheng, *Phys. Rev. B* **81**, 214115 (2010).
- [47] N. Shamir, H. Shaked, and S. Shtrikman, *Phys. Rev. B* **24**, 6642 (1981).
- [48] N. Shamir, H. Shaked, and S. Shtrikman, *Physica B+C (Amsterdam)* **90**, 211 (1977).
- [49] M. Taheri, F. S. Razavi, Z. Yamani, R. Flacau, P. G. Reuvekamp, A. Schulz, and R. K. Kremer, *Phys. Rev. B* **93**, 104414 (2016).
- [50] E. Bertaut, *J. Appl. Phys.* **33**, 1138 (1962).
- [51] E. Bertaut, *Acta Crystallogr. A* **24**, 217 (1968).
- [52] N. K. C. Muniraju, Crystal and spin structure and their relation to physical properties in some geometrical and spin spiral multiferroics, Ph.D. thesis, Forschungszentrum Jülich, 2012.
- [53] P. Mandal, C. Serrao, E. Suard, V. Caignaert, B. Raveau, A. Sundaresan, and C. Rao, *J. Solid State Chem.* **197**, 408 (2013).
- [54] W. Koehler and R. Moon, *Phys. Rev. Lett.* **29**, 1468 (1972).
- [55] A. Stewart, *Phys. Status Solidi B* **52**, K1 (1972).
- [56] S. Blundell, *Magnetism in Condensed Matter* (Oxford University, Oxford, 2003).
- [57] S. Lübeck and P. C. Heger, *Phys. Rev. Lett.* **90**, 230601 (2003).
- [58] T. Chatterji, S. Ghosh, A. Singh, L. P. Regnault, and M. Rheinstädter, *Phys. Rev. B* **76**, 144406 (2007).
- [59] H. Horner and C. Varma, *Phys. Rev. Lett.* **20**, 845 (1968).
- [60] K. Tsushima, K. Aoyagi, and S. Sugano, *J. Appl. Phys.* **41**, 1238 (1970).
- [61] E. Dobretsova, K. Boldyrev, M. Popova, S. Y. Gavrillkin, A. Mukhin, V. Y. Ivanov, V. Maltsev, N. Leonyuk, and B. Malkin, in *EPJ Web of Conferences* (EDP Sciences, Les Ulis, France, 2017), Vol. 132, p. 02008.
- [62] C. Bradley and A. Cracknell, *The Mathematical Theory of Symmetry in Solids: Representation Theory for Point Groups and Space Groups* (Oxford University, Oxford, 2010).
- [63] Y. A. Izyumov and O. V. Gurin, *J. Magn. Magn. Mater.* **36**, 226 (1983).
- [64] Y. A. Izyumov and V. Naish, *J. Magn. Magn. Mater.* **12**, 239 (1979).